Materials Characterization 204 (2023) 113224

Contents lists available at ScienceDirect

Materials Characterization

journal homepage: www.elsevier.com/locate/matchar

Cation inversion in slag magnetite: Energy loss measurements of Fe-L_3 edge shift between atom columns

Hassan Gezzaz [a,*], Cristiana L. Ciobanu [a], Ashley Slattery [b], Nigel J. Cook [a], Kathy Ehrig [a,c]

[a] School of Chemical Engineering, The University of Adelaide, Adelaide, SA 5005, Australia
[b] Adelaide Microscopy, The University of Adelaide, Adelaide, SA 5005, Australia
[c] BHP Olympic Dam, 10 Franklin Street, Adelaide, SA 5000, Australia

ARTICLE INFO

Keywords:
Magnetite
Cation inversion
EELS-STEM
Smelter slags
Trace elements

ABSTRACT

Determination of cation disorder in inverse spinels like magnetite, Fe_3O_4, is of broad interest for applications in green technologies, storage devices, and nuclear waste management since cation distributions govern magnetic and electrical properties. Magnetite is a main component of slags produced by smelting of copper ores and contains potentially valuable trace elements. We address cation disorder as a factor controlling the behavior of these elements during atmospheric cooling from 1300 °C. To estimate cation disorder, we combine atomic-scale scanning transmission electron microscopy with electron energy loss spectroscopy. The inversion parameter (0.72) indicates minor partial ordering due to fast cooling from high temperature, resulting in skeletal textures. Trace element incorporation into magnetite, instead of exsolution of discrete nanoparticle phases is promoted. Our findings provide insights into the cooling behavior of spinels and facilitate robust thermodynamic modeling that addresses the stability of structures during cooling from melts. Findings carry implications for critical element recovery and prospects for transforming industrial waste into future resources.

1. Introduction

Magnetite (Fe_3O_4) is a member of the spinel group of minerals [1]. The phase forms complex solid solutions series with the general formula:

$$^{T}(A_{1-i}B_i)^{M}[A_iB_{2-i}]O_4, \quad (1)$$

where A can be Fe^{2+}, Mg^{2+}, Mn^{2+}, Co^{2+}, Ni^{2+}, Zn^{2+}, Cu^{2+}, Ti^{4+}, Si^{4+}, Ge^{4+}, B is Fe^{3+}, Al^{3+}, Cr^{3+}, V^{3+}, i is the inversion factor, and T and M are tetrahedral and octahedral sites, respectively. Magnetite is representative of the inverse spinel structure ($i = 1$) and well known for its magnetic properties [2]. However, a completely disordered structure ($i = 0.66$) is observed in high temperature magnetite, formed close to the melting point, ~1450 °C [3]. In spinel solid solution series, the inversion factor is important as it correlates magnetic properties with crystal chemistry [4]. Spinel chemistry has attracted substantial research interest during the emergence of green technologies and the accelerating search for smart solutions to environmental issues. Current topics of spinel research range from cation disorder in Co-, Ni-, or Zn-bearing 'frustrated' spinels, the effects of Ce-doping for memory storage devices, or the use of Fe-oxides for removal of toxic pollutants, and as a sequestration host for nuclear waste [5–11].

A novel method for determining cation disorder in magnetite using electron energy loss spectroscopy (EELS) – scanning transmission electron microscopy (STEM) was proposed by Torruella et al. [12]. The method uses atomic-scale measurements of the Fe-L_3 energy loss shift along specific atom-packed directions in magnetite and thus provides a powerful tool for in-situ cation disorder characterization. Here, we apply EELS-STEM to determine the inversion factor in magnetite in slags produced during smelting of a copper concentrate from the mining-smelting-refinery operation at Olympic Dam, South Australia. Like the complex copper-uranium-silver-gold ores mined at Olympic Dam [13], magnetite and other slag phases contain a variety of critical elements, including Co, rare earth elements (REE), V, and Nb. We aim to understand the cation disorder in magnetite as a factor controlling the behavior of these elements during cooling. Phase characterization is a first step in ongoing assessment of ore-to-metal deportment of critical elements and the prospects for transforming present waste such as slags into future resources.

* Corresponding author.
E-mail address: hassan.gezzaz@adelaide.edu.au (H. Gezzaz).

https://doi.org/10.1016/j.matchar.2023.113224
Received 17 April 2023; Received in revised form 3 July 2023; Accepted 29 July 2023
Available online 31 July 2023

2. Materials and methods

The analyzed material is obtained from slags produced in an electric furnace operated at 1300 °C under reducing conditions (graphite lenses used in the furnace). These are the final stage products of the Outokumpu-process used for smelting of Olympic Dam copper sulfide concentrates. Thin polished sections (10 cm × 4 cm × 1 mm) were prepared from slag slabs cooled under atmospheric conditions in a surface bay. These were analyzed under reflected light on a Nikon petrographic microscope prior to selection of a sample of interest for nanoscale study. Identification of phases and their relative proportions was obtained by Automated Mineralogy mapping on a Hitachi SU3800 scanning electron microscope.

High-resolution transmission electron microscope analysis was carried out on two thinned (<100 nm) foils prepared in-situ from the surface of the section. Each was extracted and attached to a copper grid using a FEI-Helios nanolab Dual Focused Ion Beam and Scanning Electron Microscope (FIB-SEM) following established procedures [14].

High angle annular dark field (HAADF) STEM imaging and EELS analysis were performed at 200 kV using an ultra-high resolution, probe-corrected, FEI Titan Themis S/TEM equipped with an energy-dispersive spectroscopy (EDS) detector and Gatan Quantum 965 EELS spectrometer. Image acquisition and EDS mapping were undertaken using Velox (v. 2.13.0.1138). CrystalMaker® (v10.5.7) was used to generate crystal structure models; STEM image simulations were created using STEM for xHREM™ (v4.1) software.

STEM imaging and EELS spectra were obtained using a beam current of 55 pa, with convergence and collection angles for spectroscopy set at 26 and 86 mrad, respectively, and at a dispersion of 0.1 eV/ch. The zero-loss peak (ZLP) FWHM was measured to be approximately 1.3 eV. Dual EELS acquisition was used to obtain both the zero loss and high loss spectra simultaneously and energy drift correction was performed for all datasets. Line scans were performed with exposure of 5E-5 s (low-loss) and 0.1 s (high-loss), and with pixel sizes of 10.4 and 9.6 pm for the $[11\bar{2}]$ and $[1\bar{1}0]$ zone axes, respectively. The region used for analysis was measured to have a thickness of ~25 nm (representing 0.3 of the electrons mean free path at 200 kV) using the zero-loss log ratio (absolute) method. In agreement with simulations of electron beam channeling in STEM [15], de-channeling effects are not significant under our experimental conditions. EELS spectra were processed using Gatan Digital Micrograph™ software (v. 3.52.3932). For each linescan, a Fourier-ratio deconvolution was performed and the spatial peak values of the intensity (amplitude) and energy of Fe-L_3 edges were extracted using a Gaussian distribution function and nonlinear least-square fitting. To assess the validity of the measurements, we also performed Lorentzian and pseudo-Voigt fitting functions and compared with data obtained from Gaussian fitting. Data for each linescan was processed using exponential smoothing with a damping factor of 0.2. The maxima and minima of Fe-L_3 intensity correlate with minima and maxima values of Fe-L_3 energy. The energy shift was calculated by eV difference of the Fe-L_3 peaks measured for each pair of atomic columns along a linescan, i.e., M-T-M/M and T-T/M for the $[11\bar{2}]$ and $[1\bar{1}0]$ zone axes, respectively. Considering the smoother patterns of the intensity plots, the energy values were read at corresponding maxima and minima values of Fe-L_3 intensity.

Data representing Fourier deconvoluted EELS spectra obtained for each type of column in a linescan (obtained from initial processing) were statistically fitted to a non-parametric Gaussian Process Regression (GPR) model using MATLAB software. Squared exponential function was selected as the appropriate Kernel function. Scale length and noise variance hyperparameters were tuned to accurately fit the experimental data. Additional explanation is provided in the Supplementary Information.

All analytical data was obtained using instruments hosted within Adelaide Microscopy at the University of Adelaide.

3. Results and discussion

3.1. Sample description and transmission electron microscopy

Magnetite with composition: $(Fe^{2+}_{7.84}Mg_{0.03}Co_{0.09})_{7.96}(Fe^{3+}_{14.89}Al_{0.99})_{15.88}(Si_{0.08}Ti_{0.07})_{0.15}O_{32}$ [16], is one of the main components (~25 vol%) of EF slags from Olympic Dam, where it is associated with fayalite, Si-rich glasses and blister copper (Fig. 1a). Alongside thousands of ppm Co (CoO ~ 0.3–0.4 wt%), other critical elements such as REE, Nb, and V occur at measurable concentrations (up to tens of ppm) in slag magnetite. Two distinct glasses are recognizable from their textures and SiO_2 content. One of these, a Si-poor variety (glass1), forms simultaneously with fayalite throughout magnetite crystallization as the slag cools. Magnetite displaying skeletal textures indicative of fast growth during cooling was targeted in this study (Fig. 1b, c) for its potential to preserve cation disorder associated with crystallization at high temperatures [5]. We sampled magnetite with textures indicative of (i) late formation relative to the fayalite-glass1 eutectic assemblage, and (ii) magnetite that co-crystallized with glass1 in fayalite (Fig. 1b-e). The direct contact between fayalite and magnetite from (ii) is marked by nucleation of discrete nanoparticles (NP) of monazite (Fig. 1f, g), a rare

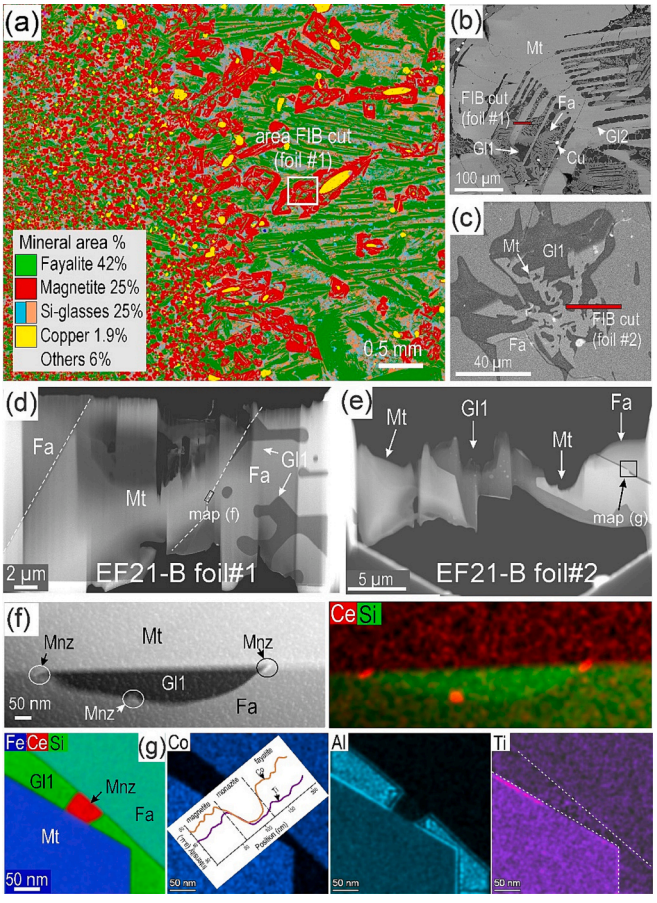

Fig. 1. Sample characterization. (a) Automated Mineralogy map showing the phase associations and their relative proportions in the slag sample. (b, c) Back scatter electron images showing location of skeletal magnetite grains (Mt) selected for nanoscale study. (d, e) HAADF STEM images of the two analyzed foils. Note that glass-fayalite symplectites, indicative of phase separation at the eutectic, are truncated by magnetite lamella (dashed line) in (d). Image (in f) and EDS STEM overlaps and element maps (f, g) showing monazite ($REEPO_4$) as NPs along magnetite grain boundaries with glass and fayalite. Profile in (g) shows variation of Co and Ti across the three phases. Note that these elements are higher in magnetite relative to fayalite. Mapped areas are marked on (d) and (e).

earth phosphate which is otherwise abundant within the early-formed glass. The EDS STEM map of the inclusion area also show homogenous distribution of the minor elements measured in magnetite at concentrations given in the formula above. Cobalt is also present in fayalite, albeit at lower concentration (Fig. 1g).

Incorporation of minor elements in the magnetite lattice is inferred from the lack of defects and an absence of discrete intragrain NPs observed during HAADF-STEM imaging of magnetite in both foils. However, NP nucleation is accompanied by formation of (110) twins at magnetite grain boundaries (Fig. 2a, b). Such twins, when in abundance, can concentrate trace elements, Si, or Si—Mg as reported for EF magnetite or skarn magnetite [16,17]. Twin planes can also assist conversion of magnetite into hematite and vice-versa [18]. Fayalite (Fig. 2c) is semi coherently oriented with magnetite (direct contact in foil #1 only), indicating a slight offset in the crystallization sequence of the two phases.

High-resolution imaging of magnetite in HAADF STEM mode shows well-defined motifs on the two zone axes, [1$\bar{1}$0] and [11$\bar{2}$] which display good spatial separation of tetrahedral (T) and octahedral (M) sites

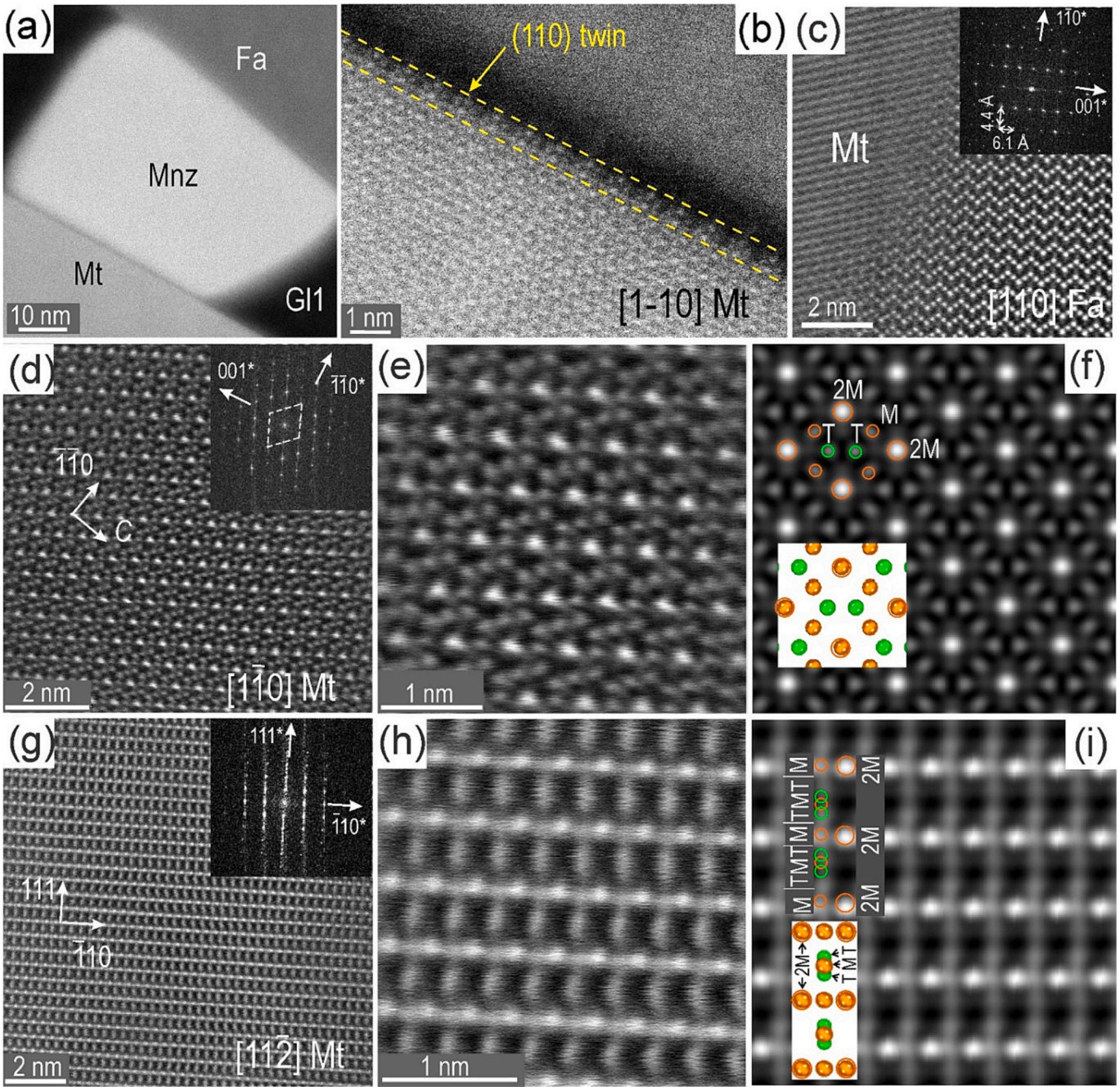

Fig. 2. HAADF STEM images and simulations in (e, h), showing magnetite and associated phases. (a) Larger monazite NP (Mnz; maps in Fig. 1g) at boundary between magnetite (Mt) and fayalite (Fa). (b) Twin along the magnetite contact with monazite in (a). (c) Fayalite adjacent to magnetite. Fast Fourier transform (FFT) pattern as inset. Note magnetite is slightly off-axis indicating non-epitaxial relationship. Magnetite tilted on two zone axes with distinct atom columns: [1$\bar{1}$0] in (d-i), and [11$\bar{2}$] in (g-i). Insets show corresponding FFT patterns. Images in (e) and (h) show the distinct motif for each of the two zone axes. These are compared with STEM simulations in (f) and (i). Brighter dots on STEM images and simulations correspond to double-atom columns of Fe in octahedral coordination (2 M), whereas the smaller dots are single Fe columns either in M or tetrahedral (T) coordination shown as overlays.

(Fig. 2c-i). STEM simulations show an excellent fit with the atomic-scale resolution images. The T and M sites are optimally separated from each other on the [1$\bar{1}$0] zone axis whereby the larger and brighter spots represent double M (2 M) atom columns relative to single M and T atom columns. The latter form a 10-atom ring around each 2 M site (Fig. 2d, f). In contrast, on the [11$\bar{2}$] zone axis, 2 M columns alternate with sequences of M-TMT columns with much tighter atom packing than the arrangement on $[1\bar{1}0]_{magnetite}$ (Fig. 2g, i). The latter zone axis resembles the [541] zone axis used in the EELS study of Torruella et al. [12], albeit with much tighter atom packing of 2 M and TMT atom columns in that case.

3.2. Magnetite crystal structure and EELS data

Magnetite (space group Fd$\bar{3}$m) is one of the 24 oxide spinels and has a crystal structure comprising cubic close packing of oxygen atoms with Fe cations occupying sites of tetrahedral and octahedral coordination (Fig. 3a). [1] Magnetite has an anomalously high electric conductivity,

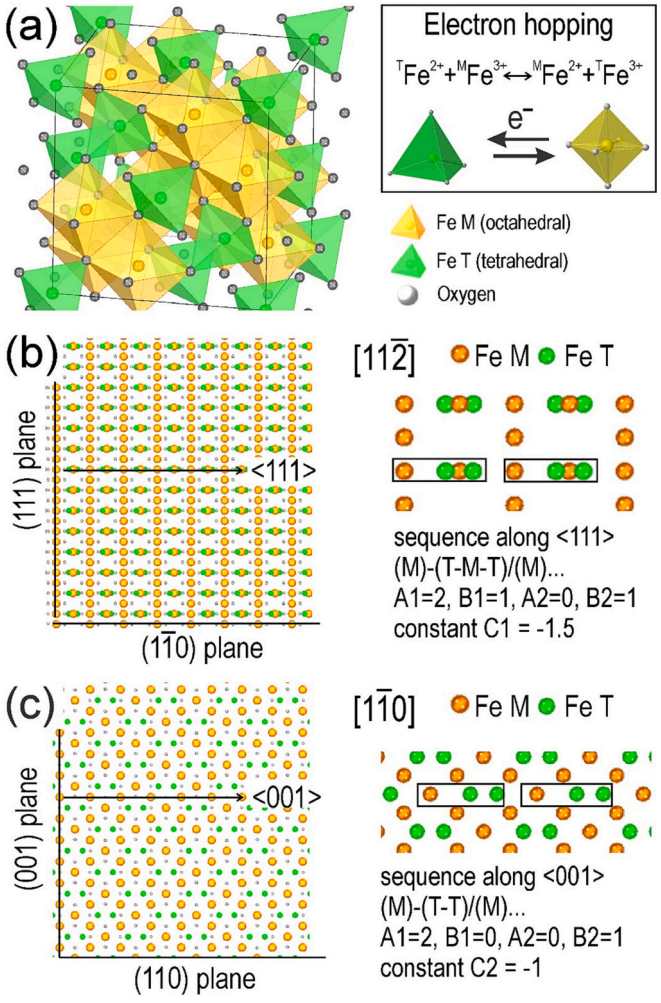

Fig. 3. Crystal structure models of magnetite. (a) Polyhedral model showing the tetrahedral (T) and octahedral (M) coordination of Fe in the unit cell. Schematic (right) for electron hopping of Fe^{2+} and Fe^{3+} between the T and M polyhedra leading to cation order/disorder. (b, c) Atom-fill models for magnetite on [11$\bar{2}$] and [1$\bar{1}$0] zone axes showing the atom columns along the <111> and < 001> directions in (b) and (c), respectively, along which the EELS measurements were conducted. The sequence of atom columns on each direction is shown (right) with parameters for calculation of the constant C according to Eq. (3) from Torruella et al. [12].

attributable to continuous exchange of electrons between Fe^{2+} and Fe^{3+} in the M sites ('electron hopping'), leading to a model of inverse spinel configuration [19], i.e., $^{T}(Fe^{3+})^{M}[Fe^{2+}Fe^{3+}]O_4$ for ideal inverse structure of magnetite with $i = 1$. The electron hopping phenomena ceases below the Verwey transition when the structure changes from a Wigner-glass to –solid, even though studies addressing magneto-electric interactions in the Fe_3O_4 multi-particle system allow definition of alternative models [2] (see also references therein).

Minor element incorporation of divalent (Co^{2+}, Mg^{2+}) and trivalent cations (e.g., Al^{3+}) is generally considered for the T and M sites, respectively. The sites hosting tetravalent substituents (e.g., Si^{4+}, Ti^{4+}, or Sn^{4+}) are debatable and dependent upon other factors [20,21].

The link between the spinel structure and the energy loss shift in Fe-L_3 between distinct atom columns in the crystal structure established by Torruella et al. [12] is a powerful atomic-scale tool to determine the inversion factor using EELS measurements. Eq. (2), from Torruella et al. [12], defines the energy for an element EELS edge (in this case Fe-L_3) at a given atom column (E_P) in correlation with the general spinel formula (1):

$$E_p = \frac{A\left[E^{2+}(1-i)+E^{3+}i\right]+B\left[E^{2+}\frac{i}{2}+E^{3+}\left(1-\frac{i}{2}\right)\right]}{A+B} \quad (2)$$

where A and B are the number of atoms of T and M coordination, respectively, within the measured column (P), energy, represented by E^{2+} and E^{3+}, are the averaged energies for the measured atom columns, and i = inversion factor. The shift between two atom columns (S) can be expressed [12] as the difference between measurements at position E_{p1} and E_{p2}, giving a formula for the i parameter as (3):

$$i = \frac{2}{3}\left(1-\frac{S}{S_{ref}}C\right), \text{where } C = \frac{(A_1+B_1)(A_2+B_2)}{B_1A_2-A_1B_2} \text{ and } S_{ref} = 1.7 \quad (3)$$

The S_{ref} parameter value is from [22].

We chose two different orientations, corresponding to the [11$\bar{2}$] and [1$\bar{1}$0] zone axes, for EELS measurements, with distribution of the T and M atoms along columns as shown in Fig. 3b and c. The energy loss shift for the Fe-L_3 edge was determined by measurements along ⟨111⟩ and ⟨001⟩ directions in magnetite with (i) a sequence of (M) and (T-M-T) atoms and (ii) (M) and (T-T). This gives a constant C1 = -1.5, the same as the experiment carried out by Torruella et al. [12], but on a different zone axis, and (ii) a different constant C2 = -1.

Representative results of the energy-loss near-edge structures (ELNES) study are shown in Figs. 4 and 5. EELS spectra taken along ~5 nm-long scanlines along <111> directions in $magnetite_{[11\bar{2}]}$ are shown in Fig. 4a and b. Ten pairs of M and T-M-T atom columns are visible on the HAADF STEM image (Fig. 4a), which are recognizable as bright and dark bands, respectively, within the EELS spectral acquisition area (Fig. 4b). There is a shift in the Fe-L_3 edge between these bands, whereby the spectral peaks for the M columns start at lower energy than those of the T-M-T columns. This shift is seen clearly in EELS spectra for the ten measurements of M and T-M-T columns along the scanline (Fig. 4c). The data was fitted for all ten spectra in each case to eliminate noise (Figs. S1, S2). In detail, the energy loss shift at the Fe-L_3 apex shows a difference of ~0.14 eV (Fig. 4d).

Quantification of the Fe-L_3 peak shift from M to T-M-T columns relative to their amplitude is given in Tables S1-S4. The correlation between high amplitude and low energy loss for each peak of individual columns is illustrated in Figs. 4e and f. The value $i = 0.733 \pm 0.005$ for the inversion factor of magnetite is obtained as an average of all scanlines, using the C1 = -1.5 constant (Fig. 4g). This value is smaller than the i value of 0.84 ± 0.02 obtained by Torruella et al. [12] for magnetite NPs from measurements on the same <111> directions but instead using the [541] zone axis with tighter atom packing. Such results are attributable to differences in the provenance and formation conditions of the magnetite samples studied (temperature, size, cooling rate; see following section).

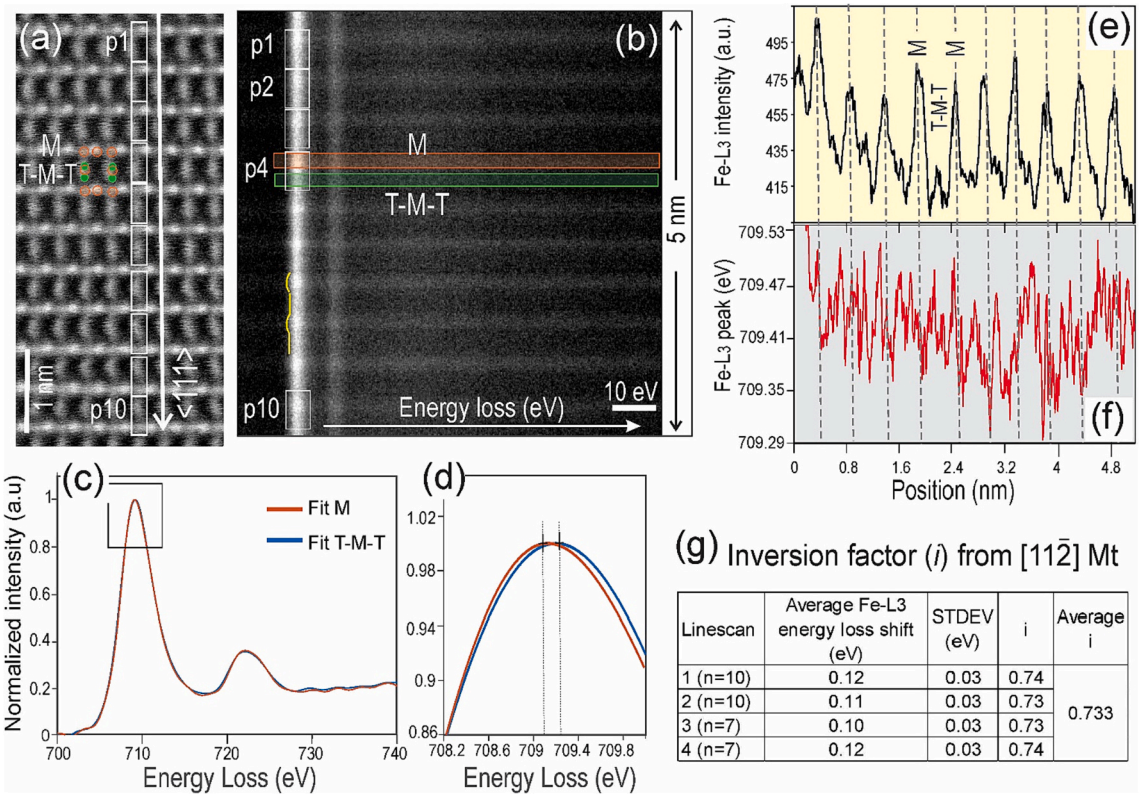

Linescan	Average Fe-L3 energy loss shift (eV)	STDEV (eV)	i	Average i
1 (n=10)	0.12	0.03	0.74	0.733
2 (n=10)	0.11	0.03	0.73	
3 (n=7)	0.10	0.03	0.73	
4 (n=7)	0.12	0.03	0.74	

Fig. 4. Energy-loss near-edge structures (ELNES) data for magnetite on [11$\bar{2}$] zone axis and corresponding values of inversion factor (*i*). (a) HAADF STEM image showing linescan 2 (arrowed) along the <111> direction in magnetite. The line contains ten pairs of atom columns (p1-p10) with M and T-M-T configurations. (b) EELS spectra bands corresponding to the pairs marked on the linescan in (a). Vertical bright lines correspond to Fe-L_3 and Fe-L_2 energy loss. Note the systematic shift of Fe-L_3 at lower energy for M columns relative to T-M-T columns (marked by the yellow line). (c) Averaged fitted EELS spectra of M and T-M-T atom columns at Fe-$L_{2,3}$ edges for linescan 2. Data representing Fourier deconvoluted EELS spectra for each type of column in the linescan were fitted using a non-parametric Gaussian Process Regression (GPR) method (Figs. S1, S2). (d) Detail from (c) showing the shift of ~0.14 eV between M and T-M-T atom columns at the Fe-L_3 edge apex. (e, f) Profiles of spatial variation of intensity and Fe-L_3 edges along linescan 2. The increment of data recording was 0.0104 nm. Peak values for position and energy corresponding to M and T-M-T columns are given in Table S2a. For comparison, measurements using Lorentzian and pseudo-Voigt fitting for the same scanline are given in Tables S2b and S2c. (g) Summary table for the inversion parameter (*i*) obtained from the four scanlines measured on [11$\bar{2}$] magnetite. The average Fe-L_3 energy loss shift is obtained from values in Tables S1-S4. Calculation of *i* using Eq. (3) and the constant C1 = -1.5. Abbreviations: M = octahedral; T = tetrahedral. (For interpretation of the references to colour in this figure legend, the reader is referred to the web version of this article.)

To further optimize this method and apply it to accurately determine the inversion factor in magnetite, we undertook the same EELS measurements on magnetite$_{[110]}$, a zone axis showing pairs of M and T-T columns along ⟨001⟩ directions (Fig. 5a). Scanlines of the same length include only five pairs, which are represented by bright and dark lines for the M and T-T columns, respectively (Fig. 5b), albeit weaker than those obtained from scanlines along <111>. Averaged EELS spectra for the five pairs show a much narrower shift for the Fe-L_3 apex (~0.08 eV compared to 0.14 eV; Fig. 5c, d). The correlation between the high amplitude and low energy loss for each peak of individual columns is illustrated in Fig. 4e and f. Quantification of the peak values is, however, spread over a larger interval (~0.25 eV; Table S5) since the data is noisier than in the first case. Although this also impacts on the correlation between maximum amplitude and minimum energy loss (Fig. 5e, f), values for the T-T pair are obtained as an average from two readings (Tables S5, S6).

Calculation of $i = 0.706 \pm 0.006$ is obtained from 13 measurements (two scanlines) and using the constant C2 = -1. This value is smaller, but close enough to the 0.733 ± 0.005 obtained from <111> directions in the same magnetite. The aggregated inversion factor obtained by combining results from the two directions is thus 0.72 ± 0.02.

3.3. Assessment of cation disorder in magnetite – consequences for thermodynamic modeling

In magnetic endmember spinels, such as magnetite, the cation distribution varies from fully inverse ($i \sim 1$) to fully disordered ($i \sim 0.66$) at ~1400 °C, as documented by thermoelectric power measurements of single crystals of magnetite at temperatures between the Curie point (~585 °C) and the melting point (~1550 °C) [3]. On the other hand, studies of cation ordering in magnetite (neutron powder diffraction) at lower temperatures (300–800 °C) have shown no significant changes of *i* below the Curie point [23] (Table S7; Fig. 6a). Our data shows slightly higher *i* than that obtained for magnetite at 1340 °C, i.e., 0.72 and 0.68 (Fig. 6a) [3], confirming our results give a robust determination of cation disorder in high temperature magnetite. The 0.04 difference lies within $\Delta i = 0.06–0.02$, the range observed for magnetite pairs studied at 600 °C and 700 °C when using different methods for measurement of *i* [3,23].

The data for magnetite nanoparticles given by Torruella et al. [12] plots well below the range of mm-sized magnetite ($\Delta i = 0.09$), both studied at ~300 °C, suggesting that magnetite particle size has an important effect on disorder in magnetite. Small differences in Δi are important when considering the interchange enthalpy (ΔH_{int}) relative to the degree of inversion using the formulae of O'Neill and Navrotsky [24] and Roelofsen et al. [5]:

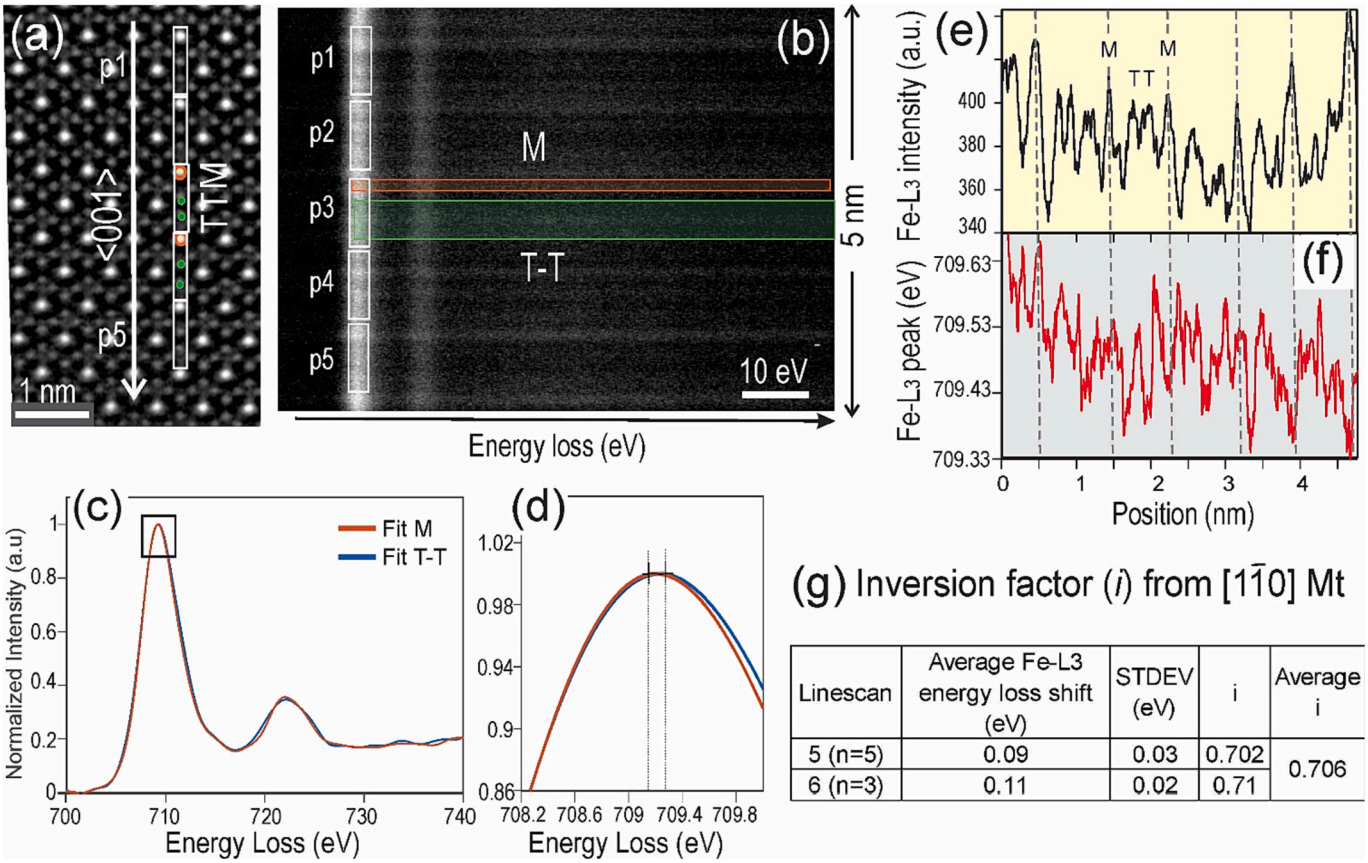

(g) Inversion factor (i) from [1$\bar{1}$0] Mt

Linescan	Average Fe-L3 energy loss shift (eV)	STDEV (eV)	i	Average i
5 (n=5)	0.09	0.03	0.702	0.706
6 (n=3)	0.11	0.02	0.71	

Fig. 5. ELNES data for magnetite on [1$\bar{1}$0] zone axis and corresponding values of inversion factor (i). (a) HAADF STEM image showing linescan 5 (arrowed) along the <001> direction in magnetite. The line contains five pairs of atom columns (p1-p5) with M and T-T configurations. (b) EELS spectra bands corresponding to the pairs marked on the linescan in (a). Vertical bright lines correspond to Fe-L_3 and Fe-L_2 energy loss. (c) Averaged fitted EELS spectra of M and T-T atom columns at Fe-$L_{2,3}$ edges for linescan 5. Data representing Fourier deconvoluted EELS spectra for each type of column in the linescan were fitted using a non-parametric GPR method (Figs. S3, S4). (d) Detail from (c) showing the shift of ~0.08 eV between M and T-T atom columns at the Fe-L_3 edge apex. (e, f) Profiles of spatial variation of intensity and Fe-L_3 edges along the linescan 5. The increment of data recording was 0.0096 nm. Peak values for position and energy corresponding to M and T-T columns are given in Table S5. (g) Summary table for the inversion parameter (i) obtained from the two scanlines measured on [1$\bar{1}$0] magnetite. The average Fe-L_3 energy loss shift is obtained from values in Tables S5–6. Calculation of i using Eq. (3) and the constant C2 = -1.

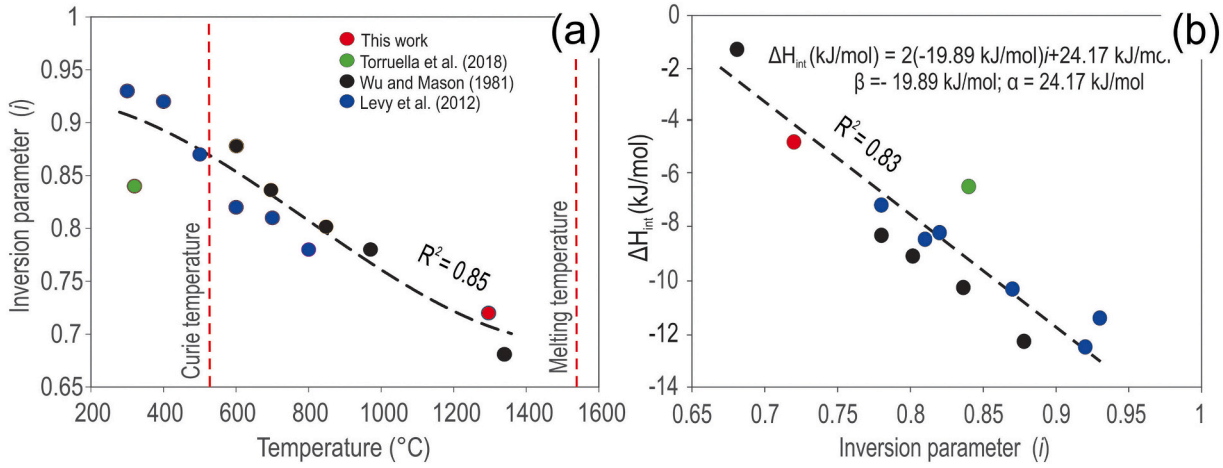

Fig. 6. Plots showing variation of inversion parameter (i) with temperature (a) and interchange enthalpy (ΔH_{int}) in (b). The values for data plotted are given in Table S7. In (a) the slag magnetite (i = 0.72; 1300 °C) plots close to another high-temperature, synthetic magnetite (i = 0.68; 1340 °C; Wu and Mason [3]). Note the highest difference between i values of magnetite formed at comparable temperatures is between magnetite NPs (i = 0.84; 320 °C; Torruella et al. [12]) and natural material (i = 0.93; 300 °C; Levy et al. [23]). In (b), the slag magnetite plots along a line between the high-temperature magnetite of Wu and Mason [3] and the lower-temperature (970–300 °C) magnetite measurements. The calculated ΔH_{int} for slag magnetite is −4.48 kJ/mol using Eq. (4) with fitted parameters, slightly higher than −4.72 kJ/mol obtained when using Eq. (4a) in which we use the furnace temperature (initially 1300 °C) rather than a measured, quenching temperature.

$$\Delta H_{int} = \alpha + 2\beta i \text{ and } (4a)\Delta H_{int} = -RT\ln\frac{i^2}{(1-i)(2-i)} \quad (4)$$

where $R = 8.314$ J/mol.K is the gas constant.

Our data supports a linear relationship between ΔH_{int} and i (Fig. 6b). The fit coefficients are the values −39.79 kJ/mol for slope and 24.17 kJ/mol for intercept. Comparing with the model by O'Neill and Navrotsky [24], we can identify the parameters $\alpha = 24.17$ kJ/mol and $\beta = -19.89$ kJ/mol for Eq. (4). These values are close to $\alpha = 17(6)$ and $\beta = -18(3)$ kJ/mol obtained for $NiAl_2O_4$ spinel Roelofsen et al. [5].

The value of ΔH_{int} obtained for the studied magnetite, ~ −5 kJ/mol, is much lower than −21 kJ/mol that would correspond to a magnetite with $i = 0.99$ at a solidification temperature of 300 °C or − 11 kJ/mol at 25 °C. To the best of our knowledge, the effect of cation disorder in specific magnetite solid solutions, like that considered here, is not included in the compound energy formalism (CEF) model used for thermodynamic calculations of phase equilibria applied to metallurgical processes [25]. Further work addressing the release of trace elements from slags containing REE and Co produced during Cu smelting will test the hypothesis of cation disorder in magnetite as an important factor when considering the Cu-Fe-O-S-Si system.

4. Conclusions and implications for critical element recovery

Recalculating the chemical formula using i = 0.72 for Fe^{3+} in the tetrahedral site (T) and based of O = 4 for simplicity, we obtain:

$$^{T}\left[(Si_{0.011}Mg_{0.004}Co_{0.012})_{\Sigma=0.026}Fe^{2+}{}_{0.254}Fe^{3+}{}_{0.72}\right]^{M}$$
$$\left[(Ti_{0.009}Al_{0.123})_{\Sigma=0.132}Fe^{2+}{}_{0.726}Fe^{3+}{}_{1.141}\right]O_4.$$

This shows the amounts of Fe^{2+} in the tetrahedral (T) site and Fe^{3+} in the octahedral site (M) to be slightly lower than 1-i (0.28), and 2-i (1.28), respectively, whereas $^{M}Fe^{2+} = 0.726$, very similar to the value of i obtained (0.72). However, by adding the sum of minor elements measured in the magnetite for each site we obtain $^{T}Fe^{2+} = 0.28$, and $^{M}Fe^{3+} = 1.273$, when considering Ti^{4+} in the M site. When present in small amounts, e.g., <0.2 a.p.f.u., Ti^{4+}, is considered to occupy the M site in preference to T [20,21]. Beyond these low concentrations, the dedicated site for Ti^{4+} is tetrahedral (as in the Ti-spinels ulvöspinel or quandilite [1].

High-temperature magnetite in magmatic-hydrothermal ore deposits or as an accessory in igneous rocks formed from natural silicate melts contains micron- to nanoscale inclusions of other spinels, among which ulvöspinel, hercynite and spinel sensu stricto are the most common [26–28]. For example, hercynite nanoparticles (NPs) are identified in magnetite formed at 670–510 ± 50 °C [28]. These carry comparable Al_2O_3 concentrations (~3.5 wt%) as that measured in slag magnetite, which lacks any NPs (Fig. 1f, g). This observation implies that cation ordering in the magnetite structure (antithetical with i) is directly correlated with cooling rates which in turn control exsolution of minor elements from spinel solid solutions. Rapidly cooled slag magnetite at atmospheric conditions undergoes skeletal growth with fayalite (Fig. 1a-c) analogous to the development of spinifex textures among silicates in high-Mg basaltic lava flows. We show this magnetite is typified by high disorder ($i = 0.72$) which acted to suppress exsolution of minor elements as discrete NPs. A further example is Co (0.3–0.4 wt% CoO), which is also retained in the magnetite structure.

Other critical elements, notably rare earths, are preferentially partitioned into glass in the slag although REE-doped magnetite NPs have been synthesized and are valued for their sensor applications [29]. Moreover, natural magnetite can retain up to thousands of ppm REE, even when formed at lower temperatures and cooled over geological time [18]. Although REE-mineral phase NPs are ubiquitous along grain boundaries, their coarsening is promoted only where defects occur in magnetite (Fig. 2a, b). Twin planes formed during cation ordering upon cooling can channel trace elements released from magnetite as well as from adjacent, coexisting slag phases. Cation ordering in magnetite and associated redistribution of minor elements could thus be important factors that will impact on design of critical element recovery methods and their feasibility.

Funding

This work was supported by the Australian Research Council through Linkage grant LP200100156 "Critical Minerals from Complex Ores" to N.J.C. and K.E., co-supported by BHP Olympic Dam.

Declaration of Competing Interest

The authors declare they have no known competing financial interests for this publication.

Data availability

All data supporting the findings of this study are available within the article (and Supporting Information).

Acknowledgements

Ben Wade and Aoife McFadden (Adelaide Microscopy) kindly assisted with electron probe microanalysis and automated mineralogy. Two anonymous reviewers are thanked for their insightful comments that helped improve clarity of the manuscript.

Appendix A. Supplementary data

Supplementary data to this article can be found online at [https://doi.org/10.1016/j.matchar.2023.113224].

References

[1] C. Biagioni, M. Pasero, The systematics of the spinel-type minerals: an overview, Am. Mineral. 99 (7) (2014) 1254–1264.
[2] F. Walz, The Verwey transition-a topical review, J. Phys. Condens. Matter 14 (12) (2002) R285.
[3] C.C. Wu, T.O. Mason, Thermopower measurement of cation distribution in magnetite, J. Am. Ceram. Soc. 64 (9) (1981) 520–522.
[4] R.J. Harrison, A. Putnis, The magnetic properties and crystal chemistry of oxide spinel solid solutions, Surv. Geophys. 19 (1998) 461–520.
[5] J.N. Roelofsen, R.C. Peterson, M. Raudsepp, Structural variation in nickel aluminate spinel (NiAl2O4), Am. Mineral. 77 (5–6) (1992) 522–528.
[6] P.F. Ndione, Y. Shi, V. Stevanovic, S. Lany, A. Zakutayev, P.A. Parilla, J.D. Perkins, J.J. Berry, D.S. Ginley, M.F. Toney, Control of the electrical properties in spinel oxides by manipulating the cation disorder, Adv. Funct. Mater. 24 (5) (2014) 610–618.
[7] D. Padalia, U.C. Johri, M.G.H. Zaidi, Effect of cerium substitution on structural and magnetic properties of magnetite nanoparticles, Mater. Chem. Phys. 169 (2016) 89–95.
[8] F.P. Fato, D.W. Li, L.J. Zhao, K. Qiu, Y.T. Long, Simultaneous removal of multiple heavy metal ions from river water using ultrafine mesoporous magnetite nanoparticles, ACS Omega 4 (4) (2019) 7543–7549.
[9] M. Ashraf, I. Khan, M. Usman, A. Khan, S.S. Shah, A.Z. Khan, K. Saeed, M. Yaseen, M.F. Ehsan, M. Tahir, N. Ullah, Hematite and magnetite nanostructures for green and sustainable energy harnessing and environmental pollution control: a review, Chem. Res. Toxicol. 33 (6) (2019) 1292–1311.
[10] E.S. Ilton, R.N. Collins, C.L. Ciobanu, N.J. Cook, M. Verdugo-Ihl, A.D. Slattery, D. J. Paterson, S.T. Mergelsberg, E.J. Bylaska, K. Ehrig, Pentavalent uranium incorporated in the structure of Proterozoic hematite, Environ. Sci. Technol. 56 (16) (2022) 11857–11864.
[11] J.R. Sandemann, T.B.E. Grønbech, K.A.H. Støckler, F. Ye, B.C. Chakoumakos, B. B. Iversen, Direct visualization of magnetic correlations in frustrated spinel $ZnFe_2O_4$, Adv. Mater. 35 (5) (2023) 2207152.
[12] P. Torruella, A. Ruiz-Caridad, M. Walls, A.G. Roca, A. López-Ortega, J. Blanco-Portals, L. López-Conesa, J. Nogués, F. Peiró, S. Estrade, Atomic-scale determination of cation inversion in spinel-based oxide nanoparticles, Nano Lett. 18 (9) (2018) 5854–5861.
[13] K. Ehrig, J. McPhie, V. Kamenetsky, Geology and mineralogical zonation of the Olympic Dam iron oxide Cu-U-Au-Ag deposit, South Australia, in: J.W. Hedenquist, M. Harris, F. Camus (Eds.), Geology and Genesis of Major Copper Deposits and Districts of the World: A Tribute to Richard H. Sillitoe 16, Society of Economic Geologists Spec. Publ, 2012, pp. 237–268.

[14] C.L. Ciobanu, N.J. Cook, S. Utsunomiya, A. Pring, L. Green, Focussed ion beam–transmission electron microscopy applications in ore mineralogy: bridging micro-and nanoscale observations, Ore Geol. Rev. 42 (1) (2011) 6–31.
[15] R.J. Wu, A. Anudha, M.L. Odlyzko, K.A. Mkhoyan, Simplifying Electron beam channeling in scanning transmission Electron microscopy (STEM), Microsc. Microanal. 23 (2017) 794–808.
[16] H. Gezzaz, C.L. Ciobanu, N.J. Cook, K. Ehrig, A.D. Slattery, B.P. Wade, A. McFadden, Silician magnetite from quenched slags formed during copper smelting, in: Proceedings, 27th Australian Conference on Microscopy and Microanalysis Perth, Western Australia, 29 January - February 2, 2023, p. 191.
[17] J. Xu, C.L. Ciobanu, N.J. Cook, A.D. Slattery, K. Ehrig, B.P. Wade, L. Courtney-Davies, L. Wang, Tin-bearing magnetite with nanoscale mg-Si defects: evidence for the early stages of mineralization in a skarn system, Front. Earth Sci. (2023) 1746.
[18] N.J. Cook, C.L. Ciobanu, K. Ehrig, A.D. Slattery, S.E. Gilbert, Micron-to atomic-scale investigation of rare earth elements in iron oxides, Front. Earth Sci. 10 (2022), 967189.
[19] E.J.W. Verwey, J.H. de Boer, Cation arrangement in a few oxides with crystal structures of the spinel type, Recueil des Travaux Chimiques des Pays-Bas. 55 (6) (1936) 531–540.
[20] P. Hernández-Gómez, K. Bendimya, C. De Francisco, C. Torres, J.M. Munoz, O. Alejos, J. Iniguez, Effect of tetravalent substitutions on the magnetic disaccommodation in magnetite, Phys. Status Solidi C 3 (9) (2006) 3180–3183.
[21] F. Bosi, U. Hålenius, H. Skogby, Crystal chemistry of the magnetite-ulvöspinel series, Am. Mineral. 94 (1) (2009) 181–189.
[22] P.A. Van Aken, B. Liebscher, V.J. Styrsa, Quantitative determination of iron oxidation states in minerals using Fe L2,3-edge electron energy-loss near-edge structure spectroscopy, Phys. Chem. Miner. 25 (1998) 323–327.
[23] D. Levy, R. Giustetto, A. Hoser, Structure of magnetite (Fe_3O_4) above the curie temperature: a cation ordering study, Phys. Phys. Chemi. Mineral. 39 (2012) 169–176.
[24] H.S.C. O'Neill, A. Navrotsky, Simple spinels; crystallographic parameters, cation radii, lattice energies, and cation distribution, Am. Mineral. 68 (1–2) (1983) 181–194.
[25] D. Shishin, E. Jak, S.A. Decterov, Thermodynamic assessment of slag–matte–metal equilibria in the cu-Fe-O-S-Si system, J. Phase Equilib. Diffus. 39 (2018) 456–475.
[26] W. Gao, C.L. Ciobanu, N.J. Cook, A. Slattery, F. Huang, D. Song, Nanoscale study of titanomagnetite from the Panzhihua layered intrusion, Southwest China: multistage exsolutions record ore formation, Minerals 9 (9) (2019) 513.
[27] C.L. Ciobanu, M.R. Verdugo-Ihl, A. Slattery, N.J. Cook, K. Ehrig, L. Courtney-Davies, B.P. Wade, Silician magnetite: Si–Fe-nanoprecipitates and other mineral inclusions in magnetite from the Olympic dam deposit, South Australia, Minerals 9 (5) (2019) 311.
[28] M.R. Verdugo-Ihl, C.L. Ciobanu, N.J. Cook, K. Ehrig, A. Slattery, L. Courtney-Davies, M. Dmitrijeva, Nanomineralogy of hydrothermal magnetite from acropolis, South Australia: genetic implications for iron-oxide copper gold mineralization, American Mineral.: J. Earth Planet. Mater. 106 (8) (2021) 1273–1293.
[29] Y. Orooji, M.H. Irani-Nezhad, R. Hassandoost, A. Khataee, S.R. Pouran, S.W. Joo, Cerium doped magnetite nanoparticles for highly sensitive detection of metronidazole via chemiluminescence assay, Spectrochim. Acta A Mol. Biomol. Spectrosc. 234 (2020), 118272.